# Observation of Electro-Optic Pockels Effect at the Amorphous $TiO_2$ and Metal Interface

Soutik Sur* and V. Venkataraman
*Department of Physics, Indian Institute of Science, Bangalore 560012, India*

(Received 10 February 2018; revised manuscript received 22 May 2018; published 23 July 2018)

The Pockels effect is theoretically forbidden in centrosymmetric media. However, centrosymmetry is broken at the interface and second-order nonlinear effects such as the Pockels effect can be detected. In this work, we report the experimental observation of the Pockels effect at the interface of two isotropic solids, amorphous sol-gel spin-coated $TiO_2$ and polycrystalline magnetron-sputtered metal. A micron-thick voltage-driven Fabry-Perot resonator is designed using these materials to experimentally detect the optical response of their interface to an applied electric field. Using the experimental data, nonlinear two-dimensional susceptibility $\chi^{(2)}_{2D}(\omega;\omega,0)$ for the interface is obtained with two different theoretical approaches and found to be $3.5 \pm 1.9 \times 10^7$ pm$^2$/V. The order of magnitude is similar to a recent report of $\chi^{(2)}_{surface}(2\omega;\omega,\omega) \sim 10^6$ pm$^2$/V for the silicon-air interface obtained from surface second-harmonic generation measurements. Isotropy usually prohibits the design of thin-film active photonic components, such as electro-optic modulators, using amorphous materials which can be deposited by simple sol-gel spin coating or sputtering. Our demonstration of the Pockels effect at the $TiO_2$ and metal interface presents it as a new electro-optic material with potential applications for integrated active plasmonic devices.

DOI: 10.1103/PhysRevApplied.10.014020

## I. INTRODUCTION

The linear electro-optic effect is forbidden in amorphous media due to its inversion symmetry [1]. This prohibits the design of active photonic components, such as electro-optic modulators, using amorphous or polycrystalline materials. However, at the interface of two centrosymmetric materials, symmetry is necessarily broken and nonlinear effects, such as surface second-harmonic generation (SSHG) $\chi^{(2)}_{surface}(2\omega;\omega,\omega)$, can be detected. This process is highly surface sensitive and enables detection of a submonolayer of molecules in most cases [2]. Another possible surface nonlinearity that has practical importance is the surface Pockels effect $\chi^{(2)}_{surface}(\omega;\omega,0)$, which has been detected recently at the air-water interface[3]. The value for the Pockels coefficient reported is large $|r| = 1.4 \times 10^5$ pm/V when compared with $|r| = 40$ pm/V of lithium niobate used in commercial electro-optic modulators [1]. The coefficient for the solid and water interface is mentioned in the literature [4] to be $|r| = 400$ pm/V. However, due to the presence of liquid, this has limited solid-state device application. In this work, we report the experimental observation of the Pockels effect at the interface of amorphous spin-coated $TiO_2$ thin film and polycrystalline magnetron-sputtered metal.

This work has potential application in integrated optics, which involves the design of miniaturized optical components such as waveguides and electro-optic modulators for compact high-speed signal processing on a small footprint [5]. Passive components such as waveguides can be fabricated using common low-cost deposition technology with amorphous and polycrystalline materials [6]. However, active components such as electro-optic modulators based on the Pockels effect are not possible because of the material isotropy. Commercial high-speed modulators are made from $LiNbO_3$ [7] and organic polymers [8], but they are not CMOS compatible [9]. Recently, electro-optic modulators have been realized with centrosymmetric silicon crystal by using its high $\chi^{(3)}$. This is an electric-field-induced second-order nonlinearity, i.e., converting high $\chi^{(3)}$ to $\chi^{(2)}$ by a dc electric field [10]. In another paper, inversion symmetry itself has been broken in silicon by adding strain in the bulk [11]. In spite of these interesting works, there is no such alternative at visible wavelengths. The Pockels effect at the spin-coated $TiO_2$ and metal interface provides a good solution. Titanium dioxide ($TiO_2$) with band gap 3.1 eV and linear index of refraction 2.3 (at 570 nm wavelength) is very suitable for transparent waveguides with tight bends for dense on-chip integration [12]. $TiO_2$ waveguides have already been realized [6,12–14] and has been reported as a promising material for nonlinear all-optical applications [12]. Waveguide modulators have also been demonstrated by combining $TiO_2$ with electro-optic polymers [15–17].

*soutik@iisc.ac.in

 

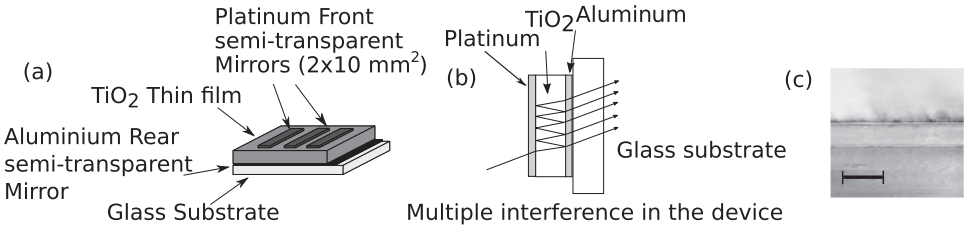


FIG. 1. (a) Device illustration. (b) Multiple beam interference effect in the device. (c) Cross section SEM image of device A (scale bar = 2 $\mu$m).

Our work presents the $TiO_2$ and metal interface as a new electro-optic material.

## II. EXPERIMENT

Micron-thick voltage-driven Fabry-Perot resonators are designed to detect the interface Pockels effect [Fig. 1(a)] and fabricated in a three-step process. First, a just over 10-nm-thick aluminum metal film is deposited on a microscope glass slide by magnetron sputtering. Then, a $TiO_2$ sol-gel precursor [18] is spin coated and subsequently annealed multiple times on a hot plate at 350°C to form about a micron-thick $TiO_2$ film. A portion of the bottom aluminum film is protected from sol-gel coating to serve as a back contact. Finally, using proper masking, less than 10 nm of platinum metal (or chromium, aluminum for comparison) was sputtered on it to make a front mirror of dimensions around $10 \times 2$ mm$^2$. Such a large-area semitransparent top electrode was required to provide a sufficiently large window for optical measurements. The sol-gel $TiO_2$ precursor [18], mentioned above, was prepared by first mixing 1 ml titanium isopropoxide (Aldrich, 97%), 9.8 ml absolute ethanol, and 6.4 $\mu$l of nitric acid ($HNO_3$, 69%), followed by adding 0.095 ml of deionized water dropwise and stirring for 12 h. A tungsten halogen lamp with a monochromator (HORIBA Jobin Yvon) was used as the light source. The monochromatic light was focused into the device by a lens. The transmitted light was collected by a large area silicon photodetector and the signal recorded as a function of wavelength. Electrical contacts were made on the semitransparent metallic layers for application of the external field.

Fabry-Perot devices with different configurations (Table I) are fabricated. For example, device A (denoted by $Pt/TiO_2/Al$) consists of platinum and aluminum front and rear semitransparent mirrors, respectively, with $TiO_2$ as the insulating dielectric. Figure 2(a) shows the transmitted light signal $I_T(\lambda)$ through this device in comparison with the measured bare-source profile $I_0(\lambda)$. Interference fringes [Fig. 1(b)] can be clearly observed in the transmitted signal. Next, we measure the change in transmitted signal $\Delta I_T(\lambda)$ by applying a bias across the device ($V_{\text{bias}}$). Since the change was small, the bias is modulated at low frequency to enable detection by a lock-in amplifier. The inset of Fig. 2(b) shows the change in transmitted signal $\Delta I_T(\lambda)$ with bias, at 570 nm wavelength. The bias modulation frequency is $f \sim 86$ Hz. We observe a linear dependence of $\Delta I_T(\lambda)$ with applied bias. Linearity is further verified by a measurement of the $2f$ (second-harmonic) component of the signal which is found to always be less than 1/10th of the fundamental. The wavelength dependence of $\Delta I_T(\lambda)$ at 5 V is shown in Fig. 2(b), which also displays clear interference fringes. Figure 3 is the two-axis plot of the normalized signals $I_T/I_0$ and $\Delta I_T/I_T$. The plot of $I_T/I_0$ clearly shows the Fabry-Perot resonances of device A. We find the $\Delta I_T/I_T$ plot also oscillates, but is phase shifted with respect to $I_T/I_0$. In addition, we note that $\Delta I_T/I_T$ at 630 nm is $\sim 0.5 \times 10^{-3}$, which is a large effect. The linearity [Fig. 2(b), inset] of this large effect confirms that it is a Pockels effect.

In the electro-optic Pockels effect, the refractive index $n(E)$ changes linearly with applied electric field $E$ [1] as $n(E) = n_0 + n_1 E + n_2 E^2 + \cdots$, where $n_1 \gg n_2 E$. Any such change in refractive index of the $TiO_2$ medium will alter the Fabry-Perot transmission coefficient and thus the

TABLE I. Experimental data for devices with different configurations. Dielectric material thicknesses for devices A, B, and C are measured using SEM and those for D–H are estimated by the fabrication process.

| Device | Configurations | Thickness (nm) | $I_T$ (at 570 nm) | $V_{\text{bias}}$ (V) | $\Delta I_T$ (at 570 nm) | $\frac{\Delta I_T}{I_T V_{\text{bias}}}$ ($V^{-1}$) |
|---|---|---|---|---|---|---|
| A | $Pt/TiO_2/Al$ | 1160 | 40 nA | 5.00 | 18.8 pA | $0.9 \times 10^{-4}$ |
| B | $Pt/TiO_2/Al$ | 860 | 25 nA | 1.00 | 6.3 pA | $2.5 \times 10^{-4}$ |
| C | $Pt/TiO_2/Al$ | 1160 | 37 nA | 5.00 | 16.5 pA | $0.9 \times 10^{-4}$ |
| D | $Pt/Spu\text{-}TiO_2/Al$ | $\sim 1000$ | 37 nA | 1.10 | 3.5 pA | $0.9 \times 10^{-4}$ |
| E | $Al/TiO_2/Al$ | $\sim 1000$ | 29 nA | 1.00 | 1.1 pA | $0.4 \times 10^{-4}$ |
| F | $Pt/TiO_2/Al$ | $\sim 1000$ | 28 nA | 1.00 | 5.0 pA | $1.8 \times 10^{-4}$ |
| G | $Cr/TiO_2/Al$ | $\sim 1000$ | 19 nA | 0.75 | 1.6 pA | $1.1 \times 10^{-4}$ |
| H | Pt/ALPO/Al | 600 | 44 nA | 5.00 | 0.6 pA | $3 \times 10^{-6}$ |

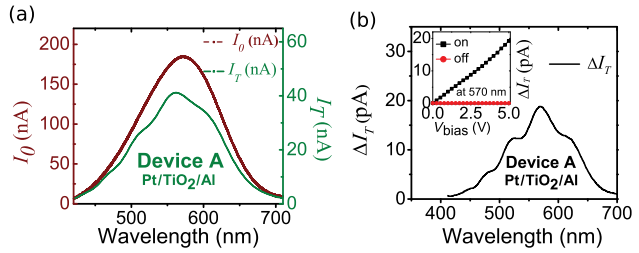


FIG. 2. (a) Source profile $I_0(\lambda)$ and transmitted light signal $I_T(\lambda)$ from device A. (b) Wavelength dependence of $\Delta I_T(\lambda)$ at $V_{\text{bias}} = 5$ V. Inset, $V_{\text{bias}}$ dependence of $\Delta I_T$. Data in black measured at wavelength 570 nm show linear dependence. Data in red are measured when the light source is off, but modulation bias and other electronics left on. This shows that the signal is not spurious and is due to the coupling of light inside the device with the bias. In the legend, on and off stand for light on and light off, respectively.

transmitted light signal. However, XRD data (Fig. 4) of $TiO_2$ deposited on silicon using the same sol-gel process does not show any sharp peaks, indicating that the film is amorphous. Since amorphous $TiO_2$ is isotropic and possesses inversion symmetry, $n(E) = n(-E)$ and $n_1$ must be zero [1] in the bulk. Hence, the bulk of $TiO_2$ can never contribute to such a linear change in transmission through the Pockels effect. However, at the $TiO_2$ and metal (aluminum or platinum) interface, the inversion symmetry is broken and a linear electro-optic phenomenon can emerge, which is otherwise absent inside the medium. This hypothesis is used for theoretical calculations later. Another possible theory from which we can obtain similar results can be a Kerr effect in the bulk in combination with the presence of a built-in electric field. Such a built-in field in the bulk of the device may be due to dissimilar electrodes (aluminum and platinum) across $TiO_2$. This field will shift the quadratic Kerr dependence and we may observe an effective linear dependence near $E = 0$. To rule this out, we measure the dc bias dependence of the $\Delta I_T$ at 557 nm, as shown in Fig. 5. A dc field with the modulating bias

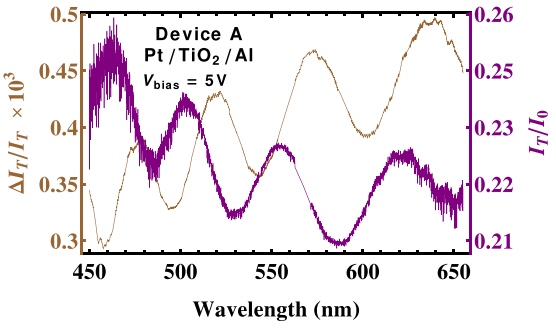


FIG. 3. Two-axis plot of normalized signals $I_T/I_0$ and $\Delta I_T/I_T$ for device A. Peak positions of the oscillations are phase shifted with respect to each other.

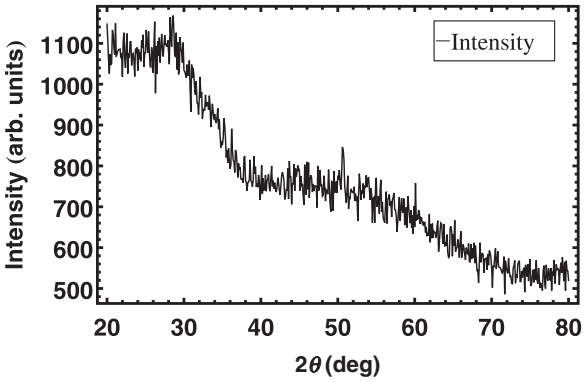


FIG. 4. XRD data of $TiO_2$ thin film on silicon wafer. No observable sharp peak shows that the deposited film is amorphous.

$V_{\text{dc}} + V_{\text{bias}} \sin(2\pi ft)$ is applied to the device for this measurement. The $V_{\text{bias}}$ in this case is 1.5 V and $f = 86$ Hz. The applied dc bias field is $\sim 1$ V/$\mu$m, which is of the order of the built-in field in the device caused by the difference in the Fermi energies of the electrodes. The flat response of $\Delta I_T$ to the dc bias voltage clearly contradicts the hypothesis of such an effective linear effect.

Experimental data for other devices with different configurations are listed in Table I and the normalized signals are compared in Fig. 6.

(1) Device B is similar to A but with different $TiO_2$ thickness while C is a replica of A to check for reproducibility.

(2) Device D is made with sputtered $TiO_2$ as the dielectric instead of sol-gel $TiO_2$. The result obtained in this case

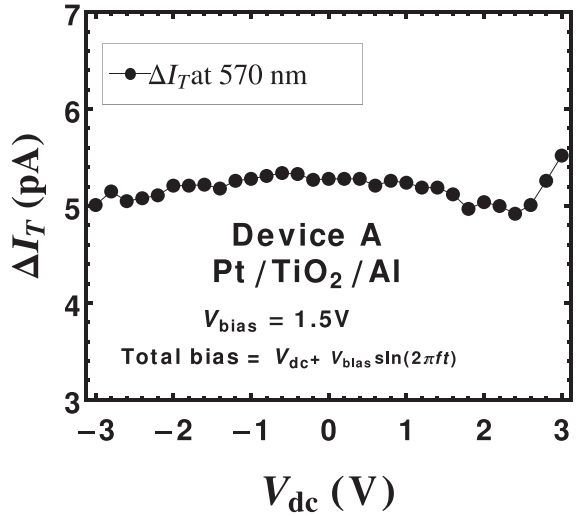


FIG. 5. dc bias dependence of device A at 570 nm incident wavelength.

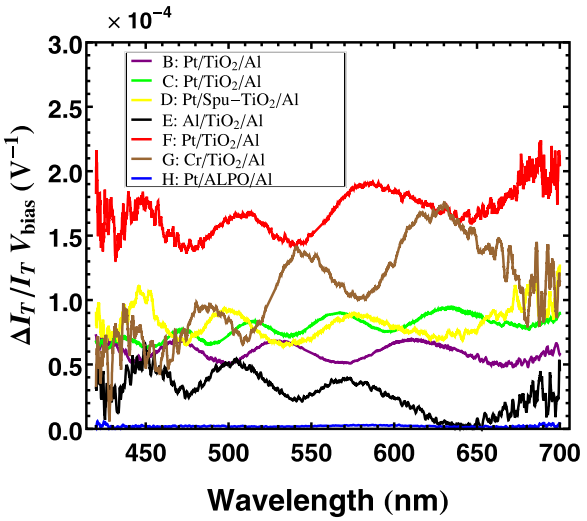


FIG. 6. Wavelength dependence of $\Delta I_T/I_T V_{\text{bias}}$ for devices listed in Table I. Aluminum phosphate oxide (ALPO) data are the blue curve, almost coinciding with the $x$ axis on this scale.

is similar to the sol-gel $TiO_2$ device. Hence, the effect is fabrication process independent.

(3) Device E is Al/$TiO_2$/Al and device F is Pt/$TiO_2$/Al. These are made from the same bottom stack (/$TiO_2$/Al). Only the top electrodes are deposited separately. So they both have $TiO_2$ as insulators with similar thickness and optical properties. This agrees with Fig. 4 where we note that the fringe pattern for devices E and F shows the same peak positions. We also notice that the signal is reduced in the device with same electrodes (aluminum). This is consistent with an interface linear effect. Since the applied electric field appears at the two interfaces in opposite directions, the change of refractive index will be of opposite signs, and they will cancel to some extent if we have similar interfaces.

(4) In device G, we replace platinum with chromium. The results are similar to Pt/$TiO_2$/Al devices.

(5) In device H, we replace $TiO_2$ with another sol-gel dielectric aluminum phosphate oxide (ALPO). ALPO is prepared following Ref. [19]. We find $\Delta I_T/I_T V_{\text{bias}}$ to be $\sim 10^{-6}$, which is two orders of magnitude lower than the value obtained from the $TiO_2$ device $\sim 10^{-4}$. This is reasonable since the third-order nonlinearity $\chi^{(3)}$ of $TiO_2$ (which is proportional to $\chi^{(2)}$ in noncentrosymmetric media) is high [1] when compared with other oxides.

All the results and experimental checks are consistent with the hypothesis of an electro-optic Pockels effect at the $TiO_2$ and metal interface. Theoretical modeling with the above hypothesis is described in the next section.

## III. THEORETICAL MODELING

We use the transfer matrix method [20] to model transmissivities of all devices. For devices A, B, and C, for example, the stratified medium consists of platinum, $TiO_2$, and aluminum as three layers, as shown in Fig. 7(a). To determine the matrix for the $TiO_2$ layer, we measured its thickness and complex dielectric constants $(n_{\text{TiO}_2} + ik_{\text{TiO}_2})$ using a SEM and ellipsometer, respectively. Ellipsometer measurements are carried out for a submicron thick layer of $TiO_2$ on silicon wafer. For metallic layers, the data for refractive index are taken from the CRC handbook [21]. The total matrix of the whole device is the product of the matrices for each layer [Eq. (1)]:

$$M = M_{\text{Pt}} \cdot M_{\text{TiO}_2} \cdot M_{\text{Al}}. \tag{1}$$

The matrix of a general layer $X$ (which can be Pt, $TiO_2$, or Al) for the electromagnetic field perpendicular to the direction of stratification is,

$$M_X = \begin{pmatrix} \cos\left(\frac{2\pi d(n+ik)}{\lambda}\right) & -\frac{i\sin\left(\frac{2\pi d(n+ik)}{\lambda}\right)}{n+ik} \\ -i(n+ik)\sin\left(\frac{2\pi d(n+ik)}{\lambda}\right) & \cos\left(\frac{2\pi d(n+ik)}{\lambda}\right) \end{pmatrix} \tag{2}$$

where $n$ and $k$ are the real and imaginary parts of the refractive index for layer $X$, $d$ is the thickness of the layer $X$, and $\lambda$ is the wavelength of light.

The transmittance for a stratified medium with total matrix $M$ is $T = |t|^2$ with Eq. (3),

$$t = \frac{2}{M_{11} + M_{12} + M_{21} + M_{22}}, \tag{3}$$

where $M_{ij}$ is the $ij$th component of the matrix $M$. Figure 8 is the plot of transmittance $T(\lambda)$ compared with the model for device A. The fitting parameters are as follows: $d_{\text{TiO}_2} = 1076$ nm, $d_{\text{Al}} = 4.3$ nm, $d_{\text{Pt}} = 5$ nm. The fitted

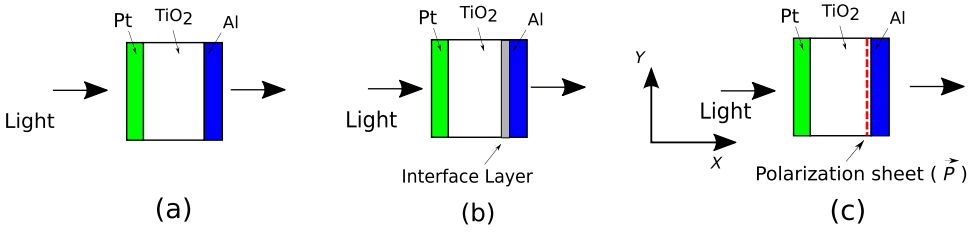


FIG. 7. (a) Model of the Fabry-Perot device with three layers as platinum, $TiO_2$, and aluminum. (b) Interface layer model (ILM) with a thin nonlinear layer at the aluminum and $TiO_2$ interface. (c) Polarization sheet model (PSM) with polarization sheet.

value of $d_{TiO_2}$ is close to the value obtained from SEM measurements.

We model the change in transmission due to the Pockels effect, $\Delta I_T/I_T$, using two different theoretical approaches, namely, the interface layer model (ILM) and the polarization sheet model (PSM). First we discuss the interface layer model.

### A. Interface Layer Model

In order to model the Pockels interface, a thin layer of $TiO_2$ of thickness $d_{layer}$ (where $d_{layer} \ll d_{TiO_2}$) with $\chi^{(2)}(\omega;\omega,0) \neq 0$ is added between aluminum and bulk $TiO_2$ [Fig. 7(b)]. We call this method the interface layer model. The refractive index of this layer will thus depend linearly on applied electric field ($V_{bias}/d_{TiO_2}$) in contrast to the bulk of $TiO_2$. The new matrix $M$ for the device is

$$M = M_{Pt} \cdot M_{TiO_2} \cdot M_{layer} \cdot M_{Al}, \tag{4}$$

where the interface layer parameters are taken to be $n_{layer} = n_{TiO_2}$ and $k_{layer} = k_{TiO_2}$ at $V_{bias} = 0$. Since $d_{layer} \ll d_{TiO_2}$, the addition of an interface layer will not change the transmissivity ($T(n_{layer},\lambda)$) of the device much. Figure 8 shows the transmittance fit with $d_{layer} = 1$ nm, which is indistinguishable from the fit without any interface layer. Now if $E_{bias}$ is the applied electric field to the device, the refractive index of the interface layer is modified as

$$n_{layer} = n_{TiO_2} + \Delta n, \quad \Delta n = \frac{\chi^{(2)}_{layer}(\omega;\omega,0)}{2n_{TiO_2}} E_{bias}. \tag{5}$$

Hence, the change in transmittance of the device $[\Delta T(n_{layer},\lambda)]$ when $\Delta n \ll n_{TiO_2}$ is

$$\Delta T = \left.\frac{\partial T}{\partial n_{layer}}\right|_{n_{layer}=n_{TiO_2}} \Delta n. \tag{6}$$

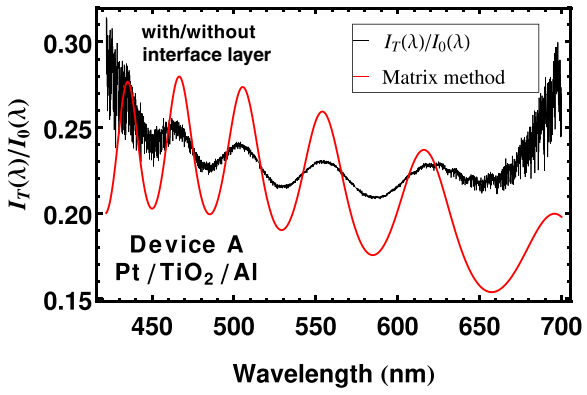


FIG. 8. Fit of transmittance $T(\lambda)$ with the transfer matrix method for device A. It remains the same even after an interface layer of thickness 1 nm is added.

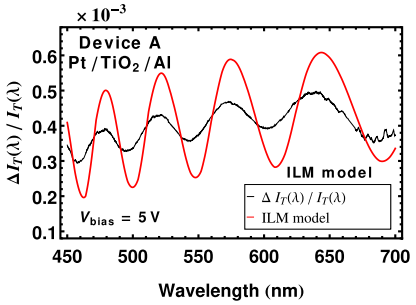


FIG. 9. Fit of normalized transmittance change $\Delta I_T/I_T$ using the ILM model.

Since

$$I_T(\lambda) = T(\lambda) I_0(\lambda), \tag{7}$$

we get

$$\frac{\Delta I_T(\lambda)}{I_T(\lambda)} = \frac{\Delta T(\lambda)}{T(\lambda)} = \frac{1}{T(\lambda)} \left.\frac{\partial T}{\partial n}\right|_{n=n_{TiO_2}} \frac{\chi^{(2)}_{layer}(\omega;\omega,0)}{2n_{TiO_2}} E_{bias} \tag{8}$$

where $\Delta I_T(\lambda)$ and $I_T(\lambda)$ are obtained from experiments. Figure 9 shows the fit of $\Delta I_T(\lambda)/I_T(\lambda)$ with the ILM model. The peak positions match the experimental data. We have earlier noted that the experimental peak positions of $\Delta I_T$ are phase shifted with respect to $I_T$ in Fig. 3. Hence, we are able to reproduce the same phase shift through the ILM model. From this fit we obtain the wavelength dependence of $\chi^{(2)}_{layer}(\omega;\omega,0)$. The value of $d_{layer}$ of 1 nm seems arbitrary at this point, but calculations show that the $\chi^{(2)}_{layer}(\omega;\omega,0)$ thus obtained varies inversely with $d_{layer}$ (Fig. 10). Therefore,

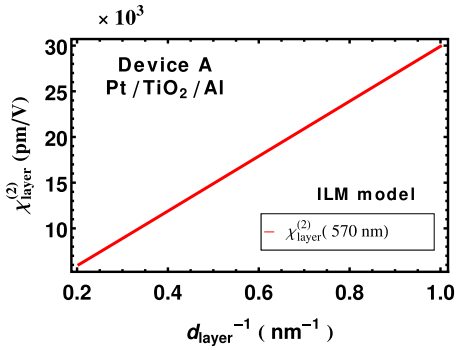


FIG. 10. Second-order susceptibility $\chi^{(2)}_{layer}$ dependence on $d_{layer}$ of device A.

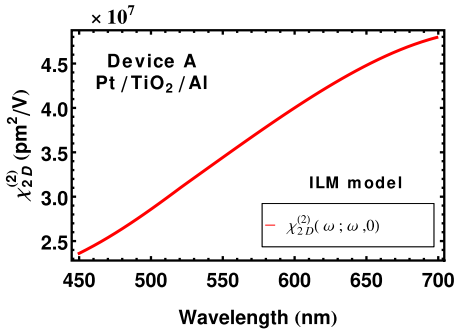


FIG. 11. Second-order susceptibility $\chi^{(2)}_{2D}$ dependence on the wavelength for device A with the ILM model.

we define $\chi^{(2)}_{2D}(\omega;\omega,0) = d_{\text{layer}}\chi^{(2)}_{\text{layer}}(\omega;\omega,0)$ as interface layer thickness-independent two-dimensional second-order susceptibility with unit $\text{pm}^2/\text{V}$. Figure 11 shows the wavelength dependence of $\chi^{(2)}_{2D}(\omega;\omega,0)$.

In order to match the oscillation amplitudes of the experimental data with the ILM (Figs. 8 and 9), we used the equidistant-phase method [22]. This takes into account partial coherence in theoretical calculations, which reduces fringe visibility. The partial coherence can be present due to a rough interface or partially coherent light source. The partially coherent layer in our case is the $TiO_2$ dielectric. We modify the matrix for this layer with an additional phase $\phi$ as

$$M_{\text{TiO}_2} = \begin{pmatrix} \cos\left(\frac{2\pi d(n+ik)}{\lambda}+\phi\right) & -\frac{i\sin\left(\frac{2\pi d(n+ik)}{\lambda}+\phi\right)}{n+ik} \\ -i(n+ik)\sin\left(\frac{2\pi d(n+ik)}{\lambda}+\phi\right) & \cos\left(\frac{2\pi d(n+ik)}{\lambda}+\phi\right) \end{pmatrix} \tag{9}$$

with $n = n_{\text{TiO}_2}$ , $k = k_{\text{TiO}_2}$, and $d = d_{\text{TiO}_2}$.

The final transmissivity of the device is the average $\langle T(\phi)\rangle$ over all possible values of $\phi$. For fully incoherent layers, $\phi$ will be random and averaging will completely suppress the oscillations in the transmission spectrum. For partial coherence, we average over three equidistant phases ($\phi = 0°, \phi = 120°$, and $\phi = 240°$) with appropriate weights [22].

$$\langle T(n_{\text{layer}},\lambda)\rangle = 0.25T(n_{\text{layer}},\lambda,120°) + 0.5T(n_{\text{layer}},\lambda,0°) + 0.25T(n_{\text{layer}},\lambda,240°). \tag{10}$$

Figure 12(a) shows the fit of $I_T/I_0$ with averaged transmittance $\langle T(\lambda)\rangle$. Figure 12(b) is the fit for experimental $\Delta I_T(\lambda)/I_T(\lambda)$ calculated using $\langle T(\lambda)\rangle$. However, such three-phase averaging does not change the obtained wavelength dependence of $\chi^{(2)}_{2D}$ [see Fig. 12(c)] when compared with Fig. 11.

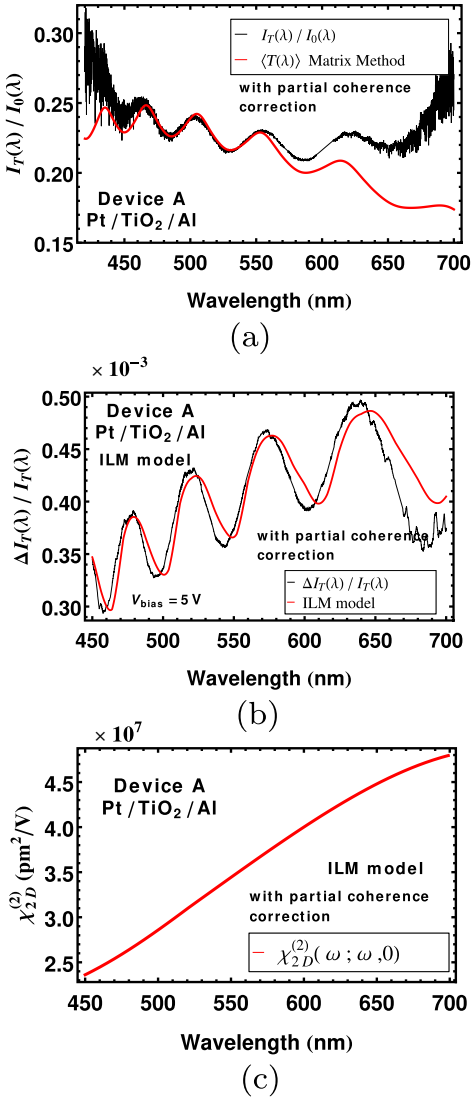


FIG. 12. (a) $\langle T(\lambda)\rangle$ fit with experiment with partial coherence for device A. (b) Fit of $\Delta I_T/I_T$ with the ILM for device A with partial coherence (c) $\chi^{(2)}_{2D}$ obtained with partial coherence for device A.

### *1. Data and fit for some other devices*

(1) Device B: The $TiO_2$ layer thickness used for the model is 762 nm. Weights used for phases 0°, 120°, and 240° are 0.62, 0.19, and 0.19, respectively. (Fig. 13)

(2) Device C: The $TiO_2$ layer thickness used for the model is 1060 nm. Weights used for phases 0°, 120°, and 240° are 0.5, 0.25, and 0.25, respectively. (Fig. 14)

## B. Polarization Sheet Model

We also use a different theoretical approach to model the Pockels effect $\Delta I_T/I_T$. This approach is typically applied for surface SHG problems [23,24]. We assume a thin sheet of polarization $P(z)\,\hat{x}$ embedded near $TiO_2$ and aluminum interface as shown in Fig. 7(c).

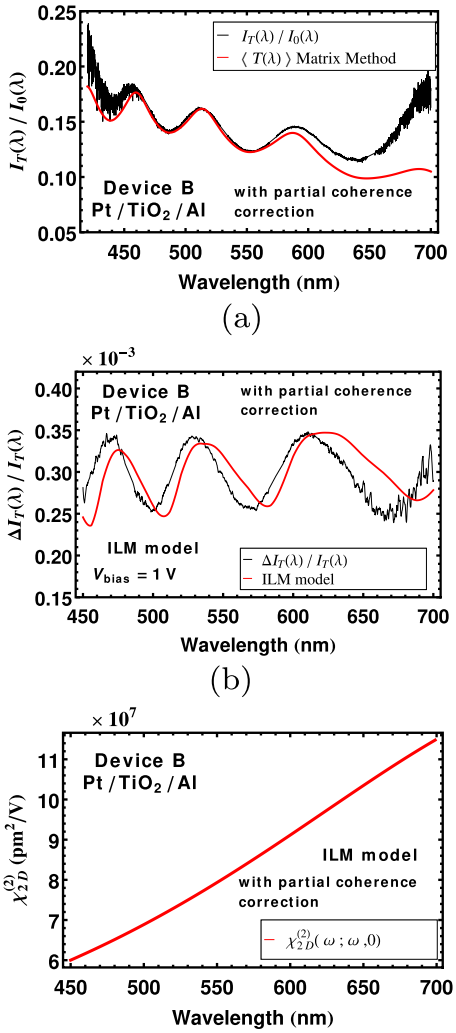


FIG. 13. (a) Fit of $I_T/I_0$ with the ILM for device B with partial coherence. (b) Fit of $\Delta I_T/I_T$ with the ILM for device B with partial coherence. (c) Wavelength dependence of $\chi^{(2)}_{2D}$ with partial coherence for device B.

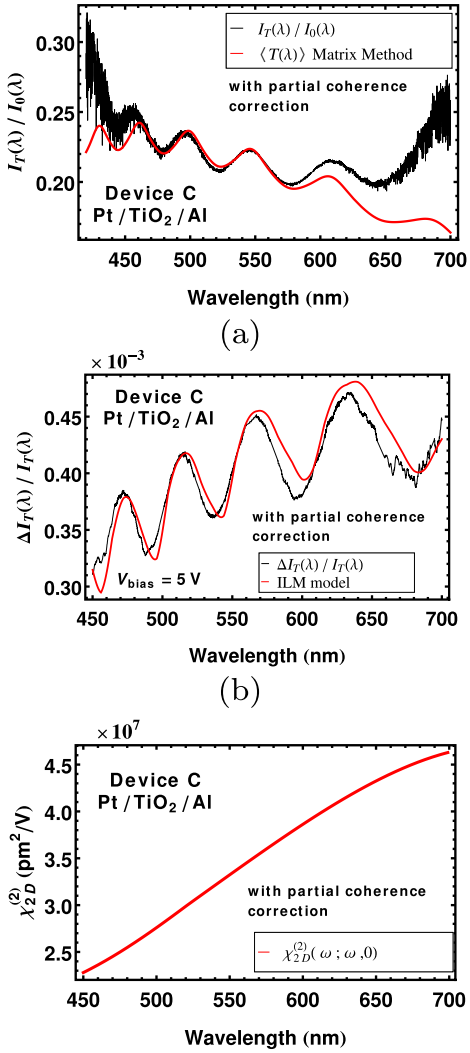


FIG. 14. (a) Fit of $I_T/I_0$ with the ILM for device C with partial coherence. (b) Fit of $\Delta I_T/I_T$ with the ILM for device C with partial coherence. (c) Wavelength dependence of $\chi^{(2)}_{2D}$ with partial coherence for device C.

The polarization sheet can be described as

$$P(z,t)\hat{x} = p\hat{x}\delta(z-z_0)e^{i\omega t}, \tag{11}$$

where $p\hat{x}$ is a position-independent polarization and $z_0$ is the location of the sheet.

Since we want to model the interface Pockels effect, we define $p$ as

$$p = \epsilon_0 \chi^{(2)}_{2D}(\omega;\omega,0)E(\omega)E_{\text{bias}}, \tag{12}$$

where $\chi^{(2)}_{2D}$ is the second-order susceptibility for the interface, $E(\omega)$ is the electric field at optical frequency $\omega$, and $E_{\text{bias}}$ is a dc field, which in our case is $V_{\text{bias}}/d_{TiO_2}$.

If the incident electric and magnetic fields are $E_0(\omega)$ and $H_0(\omega)$, respectively, then the fields at $z_0$ can be evaluated by solving Eq. (13),

$$\begin{pmatrix} E(\omega) \\ H(\omega) \end{pmatrix} = (M_{\text{Pt}} \cdot M_{\text{TiO}_2})^{-1} \begin{pmatrix} E_0(\omega) \\ H_0(\omega) \end{pmatrix} \tag{13}$$

The polarization sheet will radiate fields $E^{\pm}(\omega)$ proportional to $E(\omega)$ in both the $+z$ and $-z$ direction with magnitude

$$E^{\pm}(\omega) = \frac{ip\omega}{2c\epsilon_0} = \frac{i\omega\chi^{(2)}_{2D}(\omega;\omega,0)E(\omega)E_{\text{bias}}}{2c}. \tag{14}$$

However, for total radiated field $E^{+}_{\text{total}}(\omega)$ propagating towards $+z$, we need to consider multiple reflections of

$E^{\pm}(\omega)$ from the two interfaces. So,

$$E^{+}_{\text{total}}(\omega) = \frac{1 + r_p \exp(\frac{2i\omega n d_{\text{TiO}_2}}{c})}{1 + r_a r_p \exp(\frac{2i\omega n d_{\text{TiO}_2}}{c})} E^{+}(\omega) + \frac{1 + r_a}{1 - r_a r_p \exp\left(\frac{2i\omega n d_{\text{TiO}_2}}{c}\right)} E^{-}(\omega), \quad (15)$$

where $r_p$ and $r_a$ are reflectivities of the platinum and aluminum interfaces, respectively, with

$$r_p = \frac{(M_{\text{Pt11}} + M_{\text{Pt12}}) n_{\text{TiO}_2} - M_{\text{Pt21}} - M_{\text{Pt22}}}{(M_{\text{Pt11}} + M_{\text{Pt12}}) n_{\text{TiO}_2} + M_{\text{Pt21}} + M_{\text{Pt22}}} \quad (16a)$$

$$r_a = \frac{(M_{\text{Al11}} + M_{\text{Al12}}) n_{\text{TiO}_2} - M_{\text{Al21}} - M_{\text{Al22}}}{(M_{\text{Al11}} + M_{\text{Al12}}) n_{\text{TiO}_2} + M_{\text{Al21}} + M_{\text{Al22}}} \quad (16b)$$

$M_{\text{Al/Pt}ij}$ is $ij$ th component of the matrix $M_{\text{Al/Pt}}$ and $n_{\text{TiO}_2}$ is the refractive index of $TiO_2$.

The transmitted field is the sum of $E_T(\omega)$ and $E^{+}_{T}(\omega)$ where

$$\begin{pmatrix} E_T(\omega) \\ H_T(\omega) \end{pmatrix} = (M_{\text{Pt}}.M_{\text{TiO}_2}.M_{\text{Al}})^{-1}.\begin{pmatrix} E_0(\omega) \\ H_0(\omega) \end{pmatrix} \quad (17)$$

and

$$\begin{pmatrix} E^{+}_{T}(\omega) \\ H^{+}_{T}(\omega) \end{pmatrix} = (M_{\text{Al}})^{-1}.\begin{pmatrix} E^{+}_{\text{total}}(\omega) \\ H^{+}_{\text{total}}(\omega) \end{pmatrix} \quad (18)$$

The transmitted intensity is given by

$$I_T = |E_T(\omega) + E^{+}_{T}(\omega)|^2, \quad (19)$$

and the term in $I_T$, which is linear in $E_{\text{bias}}$, is

$$E^{+}_{T}(\omega).E_T(\omega)^* + \text{c.c.} = \frac{i\omega\chi^{(2)}_{2D}(\omega;\omega,0)E(\omega)E_{\text{bias}}}{2c} E_T(\omega)^* + \text{c.c.} \quad (20)$$

In our case $E_T(\omega) \gg E^{+}_{T}(\omega)$, so

$$I_T \sim |E_T(\omega)|^2 \quad (21)$$

Now the change in $I_T$ with $E_{\text{bias}}$ applied is

$$\Delta I_T = \frac{i\omega\chi^{(2)}_{2D}(\omega;\omega,0)E(\omega)E_{\text{bias}}}{2c} E_T(\omega)^* + \text{c.c.} \quad (22)$$

Finally,

$$\frac{\Delta I_T(\omega)}{I_T(\omega)} = \left(\frac{i\omega\chi^{(2)}_{2D}(\omega;\omega,0)E(\omega)E_{\text{bias}}}{2c} E_T(\omega)^* + \text{c.c.}\right) \Big/ |E_T(\omega)|^2 \quad (23)$$

Figure 15(a) shows the fit of experimental $\Delta I_T(\omega)/I_T(\omega)$ with the PSM without partial coherence correction. From this fit, we obtain the wavelength dependence of $\chi^{(2)}_{2D}(\omega;\omega,0)$ [Fig. 15(b)]. See the Supplemental Material [25] for the theoretical fits of devices B and C.

To summarize the theoretical section, we use the transfer matrix method to calculate transmissivity $T = I_T/I_0$ of the Fabry-Perot devices [Figs. 8, 12(a), 13(a), and 14(a)]. Modeling is performed using two theoretical methods. In the interface layer model, we added a $TiO_2$ thin layer of thickness $d_{\text{layer}}$ with nonzero $\chi^{(2)}$ between aluminum and bulk $TiO_2$ and calculated the change in transmission $\Delta T$ by modulating its refractive index. From the fits of $\Delta I_T/I_T$, $\chi^{(2)}_{\text{layer}}$ for this thin layer is obtained. Since, $d_{\text{layer}}$ is uncertain from our experiments, a two-dimensional susceptibility $\chi^{(2)}_{2D}$ is defined using the proportionality relation shown in Fig. 10.

The polarization sheet model is generally applied in the literature for surface second-harmonic generation modeling [23]. We implement the PSM for the interface Pockels effect after some modifications. The value of interface $\chi^{(2)}_{2D}$ at 570 nm obtained from both the models for all devices are summarized in Table II. The theoretical fits of the experimental data for all devices are present in the Supplemental Material [25].

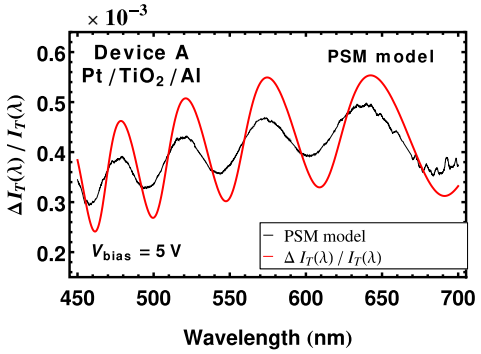


(a)

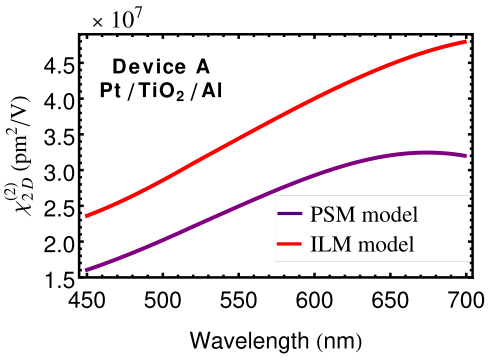


(b)

FIG. 15. (a) Fit of $\Delta I_T/I_T$ with the PSM for device A without partial coherence correction .(b) Wavelength dependence of $\chi^{(2)}_{2D}$ without partial coherence correction with the PSM and the ILM.

TABLE II. The values of $\chi^{(2)}_{2D}$ for all devices found from theoretical fits. The value of $\chi^{(2)}_{2D}$ obtained from the devices with Pt-Cr/$TiO_2$/Al configurations (devices A, B, C, D, F, and G) is $4.3 \pm 2.2 \times 10^7$ $pm^2/V$ at 570 nm with the ILM and is $2.7 \pm 1.3 \times 10^7$ $pm^2/V$ with the PSM. While combining both models, $\chi^{(2)}_{2D}$ is $3.5 \pm 1.9 \times 10^7$ $pm^2/V$. Devices E and H are not considered in the mean calculation as they are prepared with alternate materials for experimental verification.

| Device | Configurations | $\chi^{(2)}_{2D}$ with ILM at 570 nm ($pm^2/V$) | $\chi^{(2)}_{2D}$ with PSM at 570 nm ($pm^2/V$) |
|---|---|---|---|
| A | Pt/$TiO_2$/Al | $3.67 \times 10^7$ | $2.67 \times 10^7$ |
| B | Pt/$TiO_2$/Al | $8.39 \times 10^7$ | $5.12 \times 10^7$ |
| C | Pt/$TiO_2$/Al | $3.54 \times 10^7$ | $2.51 \times 10^7$ |
| D | Pt/Spu-$TiO_2$/Al | $2.13 \times 10^7$ | $1.49 \times 10^7$ |
| E | Al/$TiO_2$/Al | $0.60 \times 10^7$ | $0.41 \times 10^7$ |
| F | Pt/$TiO_2$/Al | $4.36 \times 10^7$ | $2.34 \times 10^7$ |
| G | Cr/$TiO_2$/Al | $3.43 \times 10^7$ | $2.04 \times 10^7$ |
| H | Pt/ALPO/Al | $0.05 \times 10^7$ | $0.03 \times 10^7$ |

We can note that, from Table II, $\chi^{(2)}_{2D} \sim 10^7$ $pm^2/V$. This is similar in order of magnitude to $\chi^{(2)}_{surface}(2\omega;\omega,0) \sim 10^6$ $pm^2/V$ reported for silicon surface obtained from SSHG measurements with the polarization sheet model [24]. One more observation was that for both the models, good fits are only obtained when we consider nonlinearity at the aluminum and $TiO_2$ interface. This is found to be true for every device. This indicates that $\chi^{(2)}_{2D}$ for the aluminum and $TiO_2$ interface is larger than that for the platinum and $TiO_2$ interface.

## IV. CONCLUSION AND DISCUSSION

In this paper, we report an experimental observation of the electro-optic Pockels effect at the interface of amorphous spin-coated $TiO_2$ and polycrystalline metal. The significant value of interface second-order susceptibility $\chi^{(2)}_{2D}(\omega;\omega,0) = 3.5 \pm 1.9 \times 10^7$ $pm^2/V$ at 570 nm (Table II), which is otherwise zero in the bulk, presents the $TiO_2$ and metal interface as a new electro-optic material. $TiO_2$ thin films can be deposited using a sol-gel spin-coating process which is fast, robust, cost effective, CMOS compatible, and possible in a normal laboratory environment. This electro-optic effect is very suitable for surface plasmon circuits [26], where light is mostly confined at the metal-dielectric interface. In the literature, there are successful demonstrations of high-speed surface plasmon modulators [27,28]. However, in these modulators, organic polymers are used as an electro-optic material, which can degrade with temperature. Spin-coated thin films of $TiO_2$, on the other hand, are inorganic and do not degrade even at high temperature (600°C) [29]. The interface of spin-coated $TiO_2$ and metal can be a low-cost inorganic alternative for such active plasmonic thin-film devices.

## ACKNOWLEDGMENTS

We thank Sandip Mondal for the ALPO sol-gel precursor solution. We also acknowledge the Center for NanoScience and Engineering (CeNSE), IISc Bengaluru, for providing fabrication and characterization facilities.

[1] Robert W. Boyd, *Nonlinear Optics* (Academic Press, Elsevier, San Diego, USA, 2003).

[2] Y. R. Shen, Surface second harmonic generation: A new technique for surface studies, Annu. Rev. Mater. Sci. **16**, 69 (1986).

[3] Yuto Suzuki, Kengo Osawa, Shunpei Yukita, Takayoshi Kobayashi, and Eiji Tokunaga, Anomalously large electro-optic Pockels effect at the air-water interface with an electric field applied parallel to the interface, Appl. Phys. Lett. **108**, 191103 (2016).

[4] Yugo Nosaka, Masashi Hirabayashi, Takayoshi Kobayashi, and Eiji Tokunaga, Gigantic optical Pockels effect in water within the electric double layer at the electrode-solution interface, Phys. Rev. B **77**, 241401 (2008).

[5] Elsa Garmire, J. M. Hammer, H. Kogelnik, and F. Zernike, *Integrated Optics*, Vol. 7 (Springer Science & Business Media, Berlin, Germany, 1975).

[6] Tahar Touam, Lamia Znaidi, Dominique Vrel, Iva Ninova-Kuznetsova, Ovidiu Brinza, Alexis Fischer, and Azzedine Boudrioua, Low loss sol-gel $TiO_2$ thin films for waveguiding applications, Coatings **3**, 49 (2013).

[7] Ed. L. Wooten, Karl M. Kissa, Alfredo Yi-Yan, Edmond J. Murphy, Donald A. Lafaw, Peter F. Hallemeier, David Maack, Daniel V. Attanasio, Daniel J. Fritz, Gregory J. McBrien, et al., A review of lithium niobate modulators for fiber-optic communications systems, IEEE J. Sel. Top. Quantum Electron. **6**, 69 (2000).

[8] Michael Hochberg, Tom Baehr-Jones, Guangxi Wang, Michael Shearn, Katherine Harvard, Jingdong Luo, Baoquan Chen, Zhengwei Shi, Rhys Lawson, Phil Sullivan, et al.,Terahertz all-optical modulation in a silicon–polymer hybrid system, Nat. Mater. **5**, 703 (2006).

[9] Chi Xiong, Wolfram H. P. Pernice, and Hong X. Tang, Low-loss, silicon integrated, aluminum nitride photonic circuits and their use for electro-optic signal processing, Nano Lett. **12**, 3562 (2012).

[10] E. Timurdogan, Christopher V. Poulton, M. J. Byrd, and M. R. Watts, Electric field-induced second-order nonlinear

optical effects in silicon waveguides, Nat. Photon. **11**, 200 (2017).

[11] Rune S. Jacobsen, Karin N. Andersen, Peter I. Borel, Jacob Fage-Pedersen, Lars H. Frandsen, Ole Hansen, Martin Kristensen, Andrei V. Lavrinenko, Gaid Moulin, Haiyan Ou, et al., Strained silicon as a new electro-optic material, Nature **441**, 199 (2006).

[12] Christopher Courtney Evans, *Nonlinear Optics in Titanium Dioxide: From Bulk to Integrated Optical Devices* (Harvard University, Cambridge, USA, 2013).

[13] R. Mechiakh, F. Meriche, R. Kremer, R. Bensaha, B. Boudine, and A. Boudrioua, $TiO_2$ thin films prepared by sol–gel method for waveguiding applications: Correlation between the structural and optical properties, Opt. Mater. **30**, 645 (2007).

[14] Lin Yang, S. Scott Saavedra, Neal R. Armstrong, and John Hayes, Fabrication and characterization of low-loss, sol-gel planar waveguides, Anal. Chem. **66**, 1254 (1994).

[15] Y. Jouane, Y. C. Chang, D. Zhang, J. Luo, A. K. Y. Jen, and Y. Enami, Unprecedented highest electro-optic coefficient of 226 pm/v for electro-optic polymer/$TiO_2$ multilayer slot waveguide modulators, Opt. Express **22**, 27725 (2014).

[16] Yasufumi Enami, Youssef Jouane, Jingdong Luo, and Alex K. Y. Jen, Enhanced conductivity of sol-gel silica cladding for efficient poling in electro-optic polymer/$TiO_2$ vertical slot waveguide modulators, Opt. Express **22**, 30191 (2014).

[17] Youssef Jouane and Yasufumi Enami, Nanolayer-transfer method of $TiO_2$ slot layers and its application for fabricating hybrid electro-optic polymer/$TiO_2$ vertical slot waveguide modulators, Opt. Laser Technol. **94**, 146 (2017).

[18] Esteban Pedrueza, José L. Valdés, Vladimir Chirvony, Rafael Abargues, Jesús Hernández-Saz, Miriam Herrera, Sergio I. Molina, and Juan P. Martńez-Pastor, Novel method of preparation of gold-nanoparticle-doped $TiO_2$ and $SiO_2$ plasmonic thin films: Optical characterization and comparison with Maxwell–Garnett modeling, Adv. Funct. Mater. **21**, 3502 (2011).

[19] Stephen T. Meyers, Jeremy T. Anderson, David Hong, Celia M. Hung, John F. Wager, and Douglas A. Keszler, Solution-processed aluminum oxide phosphate thin-film dielectrics, Chem. Mater. **19**, 4023 (2007).

[20] Max Born and Emil Wolf, *Principles of Optics: Electromagnetic Theory of Propagation, Interference and Diffraction of Light* (Cambridge University Press, Cambridge, UK, 1999).

[21] William M. Haynes, *CRC Handbook of Chemistry and Physics* (CRC Press, Boca Raton, USA, 2014).

[22] Rudi Santbergen, Arno H. M. Smets, and Miro Zeman, Optical model for multilayer structures with coherent, partly coherent and in coherent layers, Opt. Express **21**, A262 (2013).

[23] Victor Mizrahi and John E. Sipe, Phenomenological treatment of surface second-harmonic generation, JOSA B **5**, 660 (1988).

[24] Sean M. Anderson and Bernardo S. Mendoza, Three-layer model for the surface second-harmonic generation yield including multiple reflections, Phys. Rev. B **94**, 115314 (2016).

[25] See Supplemental Material at https://link.aps.org/supplemental/10.1103/PhysRevApplied.10.014020 for the theoretical fits of the experimental data of all devices.

[26] Stefan Alexander Maier, *Plasmonics: Fundamentals and Applications* (Springer Science & Business Media, New York, USA, 2007).

[27] A. Melikyan, L. Alloatti, A. Muslija, D. Hillerkuss, P. C. Schindler, J. Li, R. Palmer, D. Korn, S. Muehlbrandt, Dries Van Thourhout, et al., High-speed plasmonic phase modulators, Nat. Photon. **8**, 229 (2014).

[28] C. Haffner, W. Heni, Y. Fedoryshyn, J. Niegemann, A. Melikyan, D. L. Elder, B. Baeuerle, Y. Salamin, A. Josten, U. Koch, et al., All-plasmonic mach–zehnder modulator enabling optical high-speed communication at the microscale, Nat. Photon. **9**, 525 (2015).

[29] Suresh C. Pillai, Pradeepan Periyat, Reenamole George, Declan E. McCormack, Michael K. Seery, Hugh Hayden, John Colreavy, David Corr, and Steven J. Hinder, Synthesis of high-temperature stable anatase $TiO_2$ photocatalyst, J. Phys. Chem. C **111**, 1605 (2007).